8-2021

Space-Charge Limited Current in Planar and Cylindrical Crossed-Field Diodes Using Variational Calculus

Adam M. Darr
Purdue University

Ranajoy Bhattacharya
Boise State University

Jim Browning
Boise State University

Allen L. Garner
Purdue University

Physics of Plasmas ARTICLE scitation.org/journal/php

Space-charge limited current in planar and cylindrical crossed-field diodes using variational calculus

Cite as: Phys. Plasmas **28**, 082110 (2021); doi: 10.1063/5.0054307
Submitted: 16 April 2021 · Accepted: 23 July 2021 ·
Published Online: 11 August 2021

Adam M. Darr,[1] Ranajoy Bhattacharya,[2] Jim Browning,[2] and Allen L. Garner[1,3,4,a)]

AFFILIATIONS

[1]School of Nuclear Engineering, Purdue University, West Lafayette, Indiana 47906, USA
[2]Department of Electrical and Computer Engineering, Boise State University, Boise, Idaho 83725, USA
[3]School of Electrical and Computer Engineering, Purdue University, West Lafayette, Indiana 47907, USA
[4]Department of Agricultural and Biological Engineering, Purdue University, West Lafayette, Indiana 47907, USA

[a)]**Author to whom correspondence should be addressed:** algarner@purdue.edu

ABSTRACT

Crossed-field space-charge limited current (CF-SCLC) represents the maximum stable current that can be produced in crossed-field devices (CFDs); prominent CFDs include magnetrons and cyclotrons, critical technologies in vacuum electronics. While planar crossed-field geometries have the most developed theoretical models, cylindrical geometries are far more common and useful in practical applications. CFDs are characterized by the strength of the externally applied magnetic field B, orthogonal (crossed) to the electric field; this is often normalized to the magnetic insulation condition, the Hull cutoff field B_H. We apply variational calculus to derive a new theoretical model for CF-SCLC for planar and cylindrical devices below and above B_H. The variational model offers a concise derivation for planar results without transforming to the time domain and gives the first analytic results from first principles for cylindrical CF-SCLC. We implement a fully three-dimensional simulation in CST Particle Studio which, in addition to additional derived simple theoretical models, explains the often overlooked experimental current scaling $\propto \left[1-(B/B_H)^2\right]^{1/2}$ which decreases to zero current as $B \to B_H^-$. These additional simple models reduce the maximum mismatch magnitude between theory and experiments or simulations by up to 68% compared to the variational model, with the most improvement at the critical limit $B \to B_H^-$. Justification for the variational model and future applications are discussed.

I. INTRODUCTION

Space-charge limited current (SCLC), the maximum stable current in a diode gap, has been studied for just over a century,[1–3] starting with independent derivations of the planar, vacuum SCLC limit by Child and Langmuir, now called the Child–Langmuir (CL) law.[4,5] Whether optimizing to extract maximum current density or minimize the ceiling on unwanted discharges, characterizing the space-charge limit is important for a given diode geometry, especially for smaller gaps approaching the micrometer regime. Langmuir also included approximations for coaxial cylindrical and concentric spherical diodes;[5] recently, a general analytic solution was found for the space-charge diode, including closed-form relations for the cylindrical and spherical current density J_{cr}.[6]

One important characteristic of SCLC is its decrease in the presence of an external magnetic field B parallel to the electrodes and perpendicular to cathode-to-anode electric field, or "crossed-field" geometry.[7] Crossed-field devices (CFDs) pervade numerous industries; examples include magnetrons for producing high power microwaves, slow-wave structures, crossed-field amplifiers for high power radar, and nuclear fusion.[8–20] Rather than traveling directly across the gap as in the absence of a magnetic field, an electron emitted from the cathode curves as it crosses the gap, with curvature increasing with increasing magnetic field. The emitted electron will reach the anode for any $B \leq B_H$, where B_H is the Hull cutoff, given by $B_H^2 = 2\,\mathrm{m\,V\,e^{-1}\,D^{-2}}$ for a planar geometry, with electron mass m, electron charge e, bias voltage V, and gap distance D. For $B > B_H$, an emitted electron fails to reach the anode, making the diode magnetically insulated; instead, an emitted electron travels cycloidally. SCLC for a planar crossed-field diode may be derived for $B < B_H$[9] and $B > B_H$.[10] Once a crossed-field diode becomes space-charge limited, the electron flow tends to collapse to laminar or turbulent Brillouin flow, where the electrons travel in the "binormal" direction perpendicular to both B and the

electric field[7,8] and fill the gap to the Brillouin hub height above the cathode. Turbulent Brillouin flow is the lowest energy state of the diode, or attractor, and electron flow will tend to this condition for any slight perturbation in the gap, such as adding a small AC modulation, external resistance, or magnetic field misalignment.[8]

Like standard SCLC theory,[1–5] crossed-field theory has increased in sophistication over the years, including the effect of initial velocity, axial tilt, AC bias modulation, relativistic effects, nonplanar geometries, the role of ions, secondary emission, and thermal effects.[21–38] Notably, many studies include cylindrical effects due to the prevalence and importance of that geometry in practical CFDs.[39–41] However, even the most fundamental theories cannot adequately explain some fundamental trends in crossed-field SCLC, especially as $B \to B_H$. The most widely accepted theory predicts SCLC asymptotically approaches $9/(4\pi) \approx 0.72$ of the CL limit, as validated by 1D-3V (one-dimensional in space, three-dimensional in velocity) particle-in-cell (PIC) simulations,[9] whereas experimental data show a clear trend toward zero.[42–51] These experimental studies could not completely describe their divergence from theory, motivating this study to apply new analytic techniques to describe crossed-field SCLC.

Recently, we derived a geometry invariant SCLC relation using variational calculus[6,52] to reformulate the differential equation for SCLC from Poisson's equation to an energy-minimizing Euler–Lagrange equation; this yielded the first fully analytic description of cylindrical and spherical SCLC.[6] The present work adapts this approach to extend crossed-field SCLC to cylindrical geometries and theoretically explain experimental trends.[42–51] Using variational calculus, our theory fully describes SCLC for both planar and cylindrical crossed-field diodes above and below B_H, with further validation using three-dimensional (3D) trajectory simulations. The physics of charged particle motion in magnetic fields is a critical area of fundamental research in plasma physics, not only for application in CFD design but also for general plasma device operation and fusion technology.[52] Such models serve as the building block for performing more comprehensive system calculations.[53] Experimental CFDs have always relied upon the most up-to-date theoretical model of their time;[42–44,50] while first principles analytic theory had previously been confined to the planar geometry, this work reports the modeling of cylindrical CFDs and provides a framework for analyzing more complicated geometries, such as slow-wave structures or Hall thrusters.

Section II outlines the derivation of the theory and introduces the simulation setup. Section III reports the results of the theory and compares to experimental data and simulations. We make concluding remarks in Sec. IV.

II. THEORY AND SIMULATION SETUP

A. Theory

We consider a grounded cathode, an anode biased to voltage V, a magnetic field $\vec{B}$ perpendicular to the resulting electric field and parallel to the cathode for both planar and cylindrical geometries, and an electron emitted from the cathode with zero initial velocity. We write Poisson's equation as

$$\nabla^2\phi = \frac{\rho}{\epsilon_0}, \tag{1}$$

with electric potential ϕ, electron charge density ρ, and vacuum permittivity ϵ_0, and continuity as

$$\vec{J} = \rho\vec{v}, \tag{2}$$

with current density $\vec{J}$ and electron velocity $\vec{v}$. When vector arrows are omitted, the magnitude is indicated (e.g., $J \equiv |\vec{J}|$). Finally, the nonrelativistic Lorentz force law is given by

$$m\frac{d\vec{v}}{dt} = e\left(\nabla\phi - \vec{v}\times\vec{B}\right). \tag{3}$$

with electron charge e, mass m, and time t. We ignore self-magnetic fields. Total energy is unaffected by $\vec{B}$; integrating (3) yields

$$\frac{1}{2}m|\vec{v}|^2 = e\phi. \tag{4}$$

While the vectors above are general, we define $\vec{B}$ parallel to the cathode in infinite planar and cylindrical geometries, which we denote with subscripts p and c, respectively. For planar diodes, we set the cathode and anode at $x = 0$ and $x = D$, respectively, and define $\vec{B}_p \equiv B\hat{z}$, which indicates $\hat{y}$ as the binormal direction. Cylindrical diodes must be treated more carefully since the cathode may be larger or smaller than the anode; generally, we set the cathode and anode at $r = R_c$, and $r = R_a$, respectively, and define $\overline{a} \equiv R_c/R_a$. As $\overline{a} \to 1$, we expect $J_c \to J_p$, as we observed for non-magnetic SCLC.[6] One may set $\vec{B}_c$ in the polar $\hat{\theta}$ and/or axial $\hat{z}$ direction; most magnetrons are designed with only B_z to direct binormal drift in $\hat{\theta}$ since v_z drift results in high leakage,[42–44] so we assume $\vec{B}_c \equiv B\hat{z}$.

Solving directly for the binormal $\hat{y}$ component of (3) in planar geometry gives

$$m\frac{d}{dt}(v_y) = e\frac{d}{dt}(xB) \to v_y(x) = \Omega x, \tag{5}$$

with cyclotron frequency $\Omega \equiv eB/m$; we assume constant B, negligible initial velocity, and negligible self-field (nonrelativistic). In cylindrical geometry with the same assumptions, the binormal $\hat{\theta}$ component of (3) yields

$$m\frac{1}{r}\frac{d}{dt}\left(r^2\frac{d\theta}{dt}\right) = e\frac{d}{dt}(rB) \to v_\theta(r) = \frac{\Omega}{2}r\left(1 - \frac{R_c^2}{r^2}\right). \tag{6}$$

Inserting (5) and (6) into (4) yields the cathode-to-anode velocities for planar and cylindrical geometries as

$$v_x(x) = \left(\frac{2e\phi}{m} - \Omega^2x^2\right)^{1/2} \tag{7a}$$

and

$$v_r(r) = \left[\frac{2e\phi}{m} - \left(\frac{\Omega r}{2}\right)^2\left(1 - \frac{R_c^2}{r^2}\right)^2\right]^{1/2}, \tag{7b}$$

respectively.

Equations (7a) and (7b) yield B_H under the conditions $v_x(D) = 0$ and $v_r(R_a) = 0$, respectively. Defining effective cylindrical gap distance $D \equiv 0.5R_a|1 - \overline{a}^2|$[43]—(the geometry under consideration disambiguates this from planar D) yields a single definition of B_H for both geometries as

$$\frac{2eV}{m} = \Omega^2D^2 \to B_H^2 = \frac{2mV}{eD^2}. \tag{8}$$

For $B > B_H$, $\rho = 0$ beyond the electron turnaround point, called the Brillouin hub, at $x = D_H$ or $r = R_H$. To find the Brillouin hub height, a fluid model is generally preferred to the single-particle orbit formulation we have used thus far since v_x or v_r vanishes due to symmetry.[54] This means (5) and (6) may be used directly in (4) to solve for ϕ in the space-charge (Brillouin flow) region to obtain

$$\phi(x) = \frac{\Omega B}{2}x^2, \tag{9a}$$

$$\phi(r) = \frac{\Omega B}{8}r^2\left(1 - \frac{R_c^2}{r^2}\right)^2 \tag{9b}$$

for planar and cylindrical geometries, respectively.

Solving (9) for the electric field $E \equiv -\nabla\phi$ in the region containing space-charge (denoted with subscript s) for planar and cylindrical geometry, respectively yields

$$E_s(x) = -\Omega B x, \tag{10a}$$

$$E_s(r) = \frac{\Omega B}{4}r\left(\frac{R_c^4}{r^4} - 1\right). \tag{10b}$$

Since the electric field is continuous ($\rho = 0$) in the vacuum region (denoted with subscript v), (10) provides a boundary condition for Laplace's equation $\nabla \cdot \vec{E} = 0$. Solving above the Brillouin hub for planar and cylindrical geometries, respectively, gives

$$E_v(x) = -\Omega B D_H, \tag{11a}$$

$$E_v(r) = \frac{\Omega B}{4}\frac{R_H^2}{r}\left(\frac{R_c^4}{R_H^4} - 1\right). \tag{11b}$$

We calculate the hub height D_H or R_H by requiring that integrating the total electric field across the gap given by (10) below the hub height and (11) above the hub height yields the potential difference of the diode given by the anode voltage V. Note "below" and "above" are cathode-ward and anode-ward, respectively, for the cylindrical case whether $R_c > R_a$ or $R_c < R_a$. Thus,

$$\frac{1}{2}B\Omega D_H^2 + B\Omega D_H(D - D_H) = V \rightarrow D_H = D\left(1 - \sqrt{1 - \left(\frac{B_H}{B}\right)^2}\right) \tag{12}$$

for planar and

$$\frac{1}{8}B\Omega R_H^2\left(1 - \frac{R_c^2}{R_H^2}\right)^2 + \frac{1}{4}B\Omega R_H^2\left(1 - \frac{R_c^4}{R_H^4}\right)\ln\left(\frac{R_a}{R_H}\right) = V \tag{13}$$

for cylindrical, which is transcendental and must be evaluated numerically. The formalisms of variational calculus require a physical quantity to be maximized or minimized; as in the case with $B = 0$, this means extremizing $P = VI$ with power P and emitted current I from an emission area A such that $I = \int JA$.[6] For a crossed-field diode, the individual components of current follow continuity, but the total magnitude $|\vec{J}|$ is not constant across the gap due to stored binormal current. In planar and cylindrical geometries, we use the binormal velocities (7) and the x and r components of (2) in (1) and (4) to obtain

$$J_p = \epsilon_0\phi_{xx}\left[\frac{2e\phi}{m} - \Omega^2x^2\right]^{1/2}, \tag{14a}$$

$$J_c = \epsilon_0\left(\phi_{rr} + \frac{1}{r}\phi_r\right)\left[\frac{2e\phi}{m} - \left(\frac{\Omega r}{2}\right)^2\left(1 - \frac{R_c^2}{r^2}\right)^2\right]^{1/2} \tag{14b}$$

for planar and cylindrical, respectively, where we have dropped the vector notation since current and velocity are co-directional and use coordinate subscripts (x, r, and, later, generalized coordinate q) to denote partial derivatives.

Since voltage is fixed, the current may be written as

$$I_p = \int J_pA = \epsilon_0\int\phi_{xx}\left[\frac{2e\phi}{m} - \Omega^2x^2\right]^{1/2} \tag{15}$$

for planar geometry and

$$I_c = \int J_cA = \epsilon_0\int(r\phi_{rr} + \phi_r)\left[\frac{2e\phi}{m} - \left(\frac{\Omega r}{2}\right)^2\left(1 - \frac{R_c^2}{r^2}\right)^2\right]^{1/2} \tag{16}$$

for cylindrical geometry, where J_p and J_c come from (14a) and (14b), respectively.

We minimize the gap energy components, (15) and (16), by transforming to the Euler–Lagrange form,[53] given by

$$\frac{\partial^2}{\partial q^2}\left(\frac{\partial f}{\partial\phi_{qq}}\right) - \frac{\partial}{\partial q}\left(\frac{\partial f}{\partial\phi_q}\right) + \frac{\partial f}{\partial\phi} = 0, \tag{17}$$

where f is the integrand of (15) or (16) and q is a generalized coordinate – in this case, x or r. Equation (17) is solved for $B < B_H$ with standard boundary conditions $\phi'(0) = 0$, $\phi(D) = V$ for a planar diode and $\phi'(R_c) = 0$, $\phi(R_a) = V$ for a cylindrical diode, where the prime denotes differentiation with respect to x for a planar diode and r for a cylindrical diode. For a symmetric electron fluid with infinite normal and binormal dimensions, the binormal velocity for $B < B_H$ is accounted for by (7); thus, we may solve (17) purely one-dimensionally since the ϕ profile arises from all space-charge even when single-particle arguments are used. For $B > B_H$, the electron trajectories become cycloidal, and all emitted electrons are collected by the cathode. For a real diode, the emitted velocity distribution has a high energy tail, which means that magnetic insulation is not absolute until some critical $B_c > B_H$; however, these "runaway" electrons are of sufficiently low probability that they should not affect emission calculations appreciably.[29] Additionally, fluid model symmetries now eliminate v_x and v_r, leaving only binormal components. The terminating boundary condition may be changed to either the voltage or electric field at the turnaround point, as described by (9)–(11), and the resulting current must be divided by two to account for the returning current from symmetry.[10] For all cases, applying (17) to (15) gives

$$\nabla^2\phi = \frac{\phi_x^2 - 2B\Omega\phi_x x + 2B\Omega\phi}{4\phi - 2B\Omega x^2} \tag{18}$$

for planar geometry, and applying (17) to (16) gives

$$\nabla^2\phi = \frac{\phi_r^2 - r\phi_r\frac{B\Omega}{2}\left[1-\left(\frac{R_c}{r}\right)^4\right] + B\Omega\phi\left[1+\left(\frac{R_c}{r}\right)^4\right] - \left(\frac{B\Omega}{4}r\right)^2\left[1-\left(\frac{R_c}{r}\right)^2\right]^4}{4\phi - \frac{B\Omega}{2}r^2\left[1-\left(\frac{R_c}{r}\right)^2\right]^2} \tag{19}$$

for cylindrical geometry.

By inspection, (18) and (19) return the expected differential equations for standard, variational SCLE when $B = 0$.[6] Solving (18) and (19) with appropriate boundary conditions for $B < B_H$ or $B > B_H$ gives SCLC at the cathode. The one-dimensionalization inherent in the derivation makes it critical to carefully account for continuity in (19) when interpreting the calculated current at any location other than the cathode. Appendix A provides details on assessing electron continuity for 1D, 2D, and 3D non-planar geometries.

We introduce the following dimensionless variables to facilitate analytic manipulation of (18) and (19): $\overline{x} = x/D$, $\overline{r} = r/R_a$, $\overline{B} = B/B_H$, $\overline{\phi} = \phi/V$, $\overline{J} = J/J_{SCLC}$, with space-charge limited current (SCLC) J_{SCLC} denoting the $B = 0$ solution[1–3] for the given geometry; note this means $\overline{R}_c = \overline{a}, \overline{R}_a = 1$ for any cylindrical geometry. Recasting (18) gives

$$\nabla^2\overline{\phi} = \frac{\overline{\phi}_{\overline{x}}^2 - 4\overline{B}^2\overline{\phi}_{\overline{x}}\overline{x} + 4\overline{B}^2\overline{\phi}}{4\overline{\phi} - 4\overline{B}^2\overline{x}^2} \tag{20}$$

for planar geometry, and (19) becomes

$$\nabla^2\overline{\phi} = \frac{\overline{\phi}_{\overline{r}}^2 - \frac{4\overline{B}^2\overline{r}\overline{\phi}_{\overline{r}}}{(1-\overline{a}^2)^2}\left[\frac{\overline{r}^4-\overline{a}^4}{\overline{r}^4}\right] + \frac{8\overline{B}^2\overline{\phi}}{(1-\overline{a}^2)^2}\left[\frac{\overline{r}^4+\overline{a}^4}{\overline{r}^4}\right] - \left(\frac{2\overline{B}\overline{r}}{(1-\overline{a}^2)^2}\right)^2\left[\frac{\overline{r}^2-\overline{a}^2}{\overline{r}^2}\right]^4}{4\overline{\phi} - \frac{4\overline{B}^2\overline{r}^2}{(1-\overline{a}^2)^2}\left[\frac{\overline{r}^2-\overline{a}^2}{\overline{r}^2}\right]^2} \tag{21}$$

for cylindrical geometry. Inserting $\overline{\phi}$ from (20) or (21) into (14a) or (14b), respectively, yields the SCLC density for a planar or cylindrical diode, respectively. Appendix B details the derivation of (20) and (21). Equations (20) and (21) are highly nonlinear; the additional magnetic field terms prevent an exact analytic solution. Furthermore, (20) and (21) can become numerically unstable as $\overline{B} \to 1$ due to the singularity at $\overline{B} = 1$.

B. Simulation setup

We performed a CST[57] particle tracking simulation for similar planar and cylindrical geometries. As shown in Fig. 1(a), for the planar geometry, we selected gap distance $D = 1$ mm, electrode width W, and length L such that $W = L = 10\,\text{mm} \gg D$ to minimize 2D and 3D effects. The cylindrical structure had $R_c = 10$ mm, $R_a = 20$ mm, with $L = 40$ mm. For the simulations, a hexahedral mesh optimization study was implemented, resulting in $>3.5 \times 10^6$ mesh cells in planar and $>4.5 \times 10^6$ in cylindrical, along with ~16 000 macroparticles to achieve solution convergence.[58] The smaller length-to-gap ratio for the cylindrical geometry mirrors prior experimental setups, which had $R_a/L \sim 1$.[43,44,50] An area particle source was defined on the entire cathode surface for both geometries. Dirichlet (open) boundary conditions are used for all simulations. Both diodes were biased to 10 kV and simulated both with and without end-hats to analyze the effect of electric field perturbation upon critical (space-charge limited) current density J_{cr}. The end-hats confine the electrons inside the simulation domain; without the end-hats, which are biased at the cathode potential, the electrons exit from the simulation structure due to space-charge. As for the theoretical studies above, we applied fixed magnetic field $\vec{B} = B\hat{z}$ for both geometries. Two methods were available to determine J_{SCLC} at $B = 0$: (1) a space-charge emission model and (2) a fixed current emission model that could be varied until achieving the standard space-charge limited condition, $E = 0$ at the cathode. While the planar diode exhibited similar results for both models, we observed differences in excess of 25% for the cylindrical diode. This was probably due to two-dimensional effects of finite length, reinforcing the decision to normalize experimental results to $B = 0$ data; the same normalization was chosen for the simulation results shown, using the fixed current emission model data.

III. RESULTS

Figure 2 shows that the full results from the variational approach (20) match exactly with existing models for planar crossed-field diodes,[9,10] and the near-planar cylindrical ($\overline{a} = 1.3^{\pm 1}$) solution (21) matches almost as closely, as expected from experiments.[42–44,50] One limitation of the numerical solutions of (21) is a failure to converge for $0.95 \lesssim \overline{B} \lesssim 1.05$ due to the singularity at $\overline{B} = 1$, especially for $\overline{a}$ far from unity (highly cylindrical). Because of the agreement between near-planar cylindrical and planar geometries from (20) and (21), respectively, the prior 1D planar theory[9,10] is recommended for practical calculations since (20) is not closed form. Since (20) and (21) match existing theory[9,10] at appropriate limits, they represent analytic, first-principles models for crossed-field SCLE in planar and more common cylindrical geometries. Examining Fig. 2 more closely, the choice of normalizing J_{cr} to J_{SCLC} means inverse and conventional magnetron geometries return the same result; that is, $\overline{R}_c$ and $\overline{R}_a$ may be interchanged, hence the single curve for $\overline{a}^{\pm 1}$. When transformed to

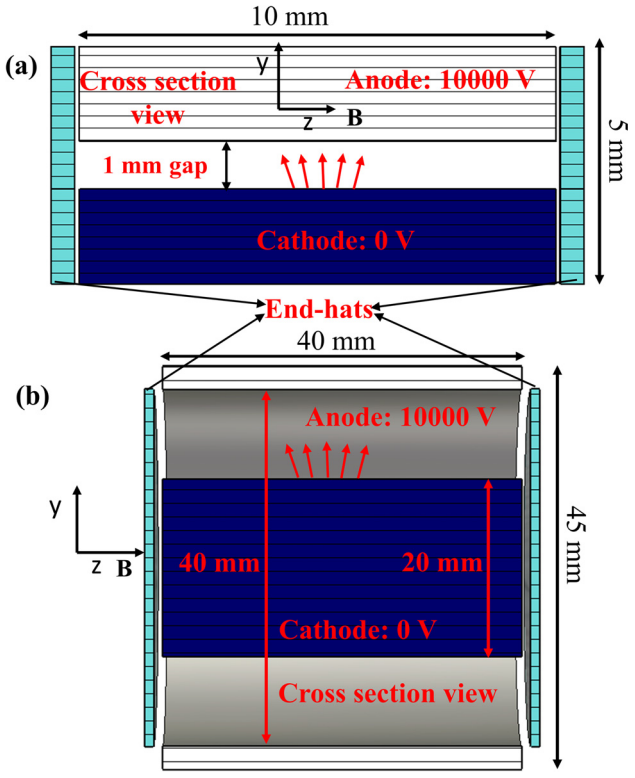

FIG. 1. Simulation geometry used for the particle tracking simulations; (a) planar geometry with end-hats and a 10×10 mm wide anode and cathode with a 1 mm gap in between. The magnetic field B is oriented in the $\hat{z}$ direction. (b) Cylindrical geometry with end-hats, 20 mm radius cathode, 40 mm radius anode, with B in $\hat{z}$. The simulations were performed both with and without end-hats for both geometries; without end-hats, significant leakage occurred at the ends of the diodes.

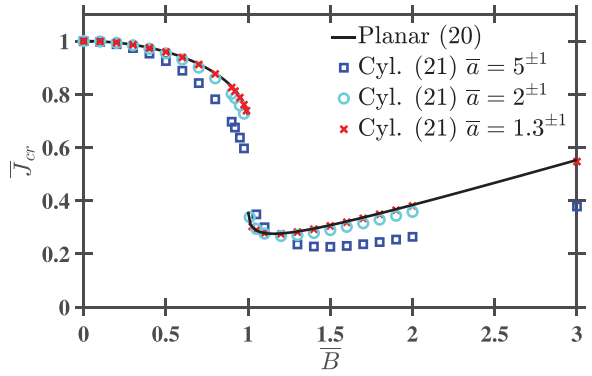

FIG. 2. Dimensionless current density $\bar{J}_{cr}$ as a function of dimensionless magnetic field $\bar{B}$, where the solid line represents the planar analytic solution (20), and the points represent solutions to (21) for cylindrical geometries with various ratios of cathode (R_c) -to-anode (R_a) radius $\bar{a} = R_c/R_a$. Due to the normalization of $\bar{J}$, the cylindrical results are identical for both conventional ($\bar{a}$) and inverted ($\bar{a}^{-1}$) magnetron geometries, that is, for $\bar{a}$ and $\bar{a}^{-1}$, expressed as $\bar{a}^{\pm 1}$, since the cathode and anode may be interchanged. The cylindrical calculations are numerically unstable for $0.95 \lesssim \bar{B} \lesssim 1.05$.

physical units, the SCLC normalizations will yield different physical values for conventional and inverted devices. Figure 2 makes the overall trend clear: increasingly cylindrical ($\bar{a}$ far from unity) diodes experience increasingly extreme deviations from J_{SCLC}, especially as $\bar{B} \to 1^-$. We observe the initial decrease in J_{cr} for planar when $\bar{B} > \bar{B}_H$, as seen in earlier 1D planar crossed-field theoretical studies,[10] mirrored in cylindrical solutions. Ultimately, at high $\bar{B} \gg 1$, the hub height becomes vanishingly small and the electrons spend accordingly less time in the gap. This causes J_{cr} to increase with increasing $\bar{B}$; since the rate of reduction of the hub height with increasing $\bar{B}$ will ultimately diminish since the hub height asymptotically approaches the cathode, J_{cr} will increase more slowly as $\bar{B} \to \infty$. Although (20) matches expected theoretical results,[9,10] it is important to acknowledge that neither this new variational model nor any of the accepted planar crossed-field models from the literature[9,10,12,13,21] explain many experimental results, clearly showing $\bar{J}_{cr} \to 0$ as $\bar{B} \to 1^-$.[42–44,50] While Fig. 2 shows these trends may occur for highly cylindrical diodes, all the experiments were for near-planar geometries with $\bar{a} \approx 1$; none of the experiments exceeded $\bar{a} = 1.3^{\pm 1}$. At the time, these experimental results were hypothesized, variously, to be the result of weak relativistic effects, inhomogeneities or misalignments in the experimental setup, or secondary emission.[42–44,50] Given the common trend among experiments with widely differing characteristics over an order of magnitude in voltage, both inverse and conventional configurations, many different gap distances, and two different research groups performing the experiments, it is unlikely that any one factor caused the trend. In fact, given that these represent the bulk of all experimental results for crossed-field SCLE for $\bar{B} < 1$, it may be possible these results are universal.

Considering Fig. 2, $\bar{J}_{cr} < 1$ for all $0 < \bar{B} < 1$. From the energy balance (4) and the velocity results (5) and (6), we also know the exact cathode-to-anode and binormal velocities at the anode. Since the total current—including stored current—cannot effectively exceed J_{SCLC} without violating the space-charge limited condition, we may estimate $|\vec{J}|_{anode} = J_{SCLC}$ and compare normal (7) and binormal (5) and (6) velocities to determine normal (collected) anode current density. Since $\vec{J}$ obeys three-dimensional continuity, $\nabla \cdot \vec{J} = 0$ over the bulk diode [as opposed to local continuity used in (16), cf. Appendix A], the normal current density at the anode may be recalculated as cathode emission current,

$$\bar{J}_{cr} = \sqrt{1 - \bar{B}^2}. \tag{22}$$

Equation (22), unlike (20), accounts for bulk, three-dimensional effects in the entire diode explicitly and matches phenomenologically based fits precisely.[44] This simple model must be used cautiously, however, as there is no guarantee that $|\vec{J}|_{anode} = J_{SCLC}$. Alternatively, we may begin by noting the similarities shown in Fig. 3 between $\bar{\phi}(\bar{x})$ from the solution of (20) and SCLC.[6] We may then compute the total average current $\langle |\vec{J}| \rangle$ in a planar gap assuming the potential profile follows the SCLC limit (CL in planar), noting $J_y/J_x = v_y/v_x$, using the velocities given by (4) and (5), and assuming $\bar{\phi}(\bar{x}) = \bar{x}^{4/3}$ as in CL,

$$\langle |\vec{J}| \rangle = \bar{J}_x \int_0^1 \sqrt{1 + (\bar{v}_y/\bar{v}_x)^2}\, d\bar{x} = \bar{J}_x \int_0^1 \left(1 - \bar{B}^2 \bar{x}^{2/3}\right)^{-1/2} d\bar{x}. \tag{23}$$

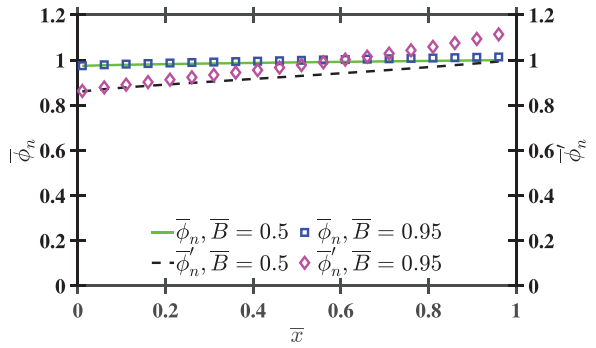

FIG. 3. Ratio of the dimensionless electric potential $\overline{\phi}$ from (20) for dimensionless magnetic fields $\overline{B}$ to the dimensionless electric potential in a non-magnetic planar space-charge limited gap $\overline{\phi}_{CL}$,[6] given by $\overline{\phi}_n \equiv \overline{\phi}/\overline{\phi}_{CL}$, and the ratio of the normalized electric field magnitudes for magnetic and non-magnetic gaps, given by $\overline{\phi}'_n \equiv (d\overline{\phi}/d\overline{x})/(d\overline{\phi}_{CL}/d\overline{x})$, as functions of $\overline{x}$ from 0 (cathode) to 1 (anode).

Evaluating (28) and comparing to J_{CL} yields a limit for planar emission current J_x as

$$\overline{J}_x = \frac{2}{3}\overline{J}_{CL}\frac{\overline{B}^3}{\sin^{-1}(\overline{B}) - \overline{B}\sqrt{1-\overline{B}^2}}, \tag{24}$$

which has the limit $\overline{J}_x \to (4\overline{J}_{CL})/(3\pi)$ as $\overline{B} \to 1^-$ and $\overline{J}_{cr} \to \overline{J}_{CL}$ as $\overline{B} \to 0$. Equation (24) is more restricted than the full solution (20); Fig. 3 shows that the CL potential is larger, resulting in a larger integral in (23) and a smaller prediction than expected in (24).

The simple analytic solutions from (22) and (24) are limited by their respective constituent assumptions; nonetheless, they capture enough of the physics to be powerful tools to model experimental results. Comparing these and the full theory from (20) [we omit (21) since the most extreme experimental $\overline{a}$ falls within $1.3^{\pm 1}$,[42–44,50] which we showed in Fig. 2 to match planar nearly perfectly] to normalized experimental data, Fig. 4 shows the full theory cannot adequately model experimental results, while the simple theories, especially (22), can. All experiments are normalized to reported data for $\overline{B} = 0$ (since some papers did not report dimensional data, we assume near-planar B_H when normalizing). The subfigures of Fig. 4 are ordered chronologically; a trend toward cleaner data is observed in later experiments. Figures 4(a)–4(c) show that experiments conducted in the 1970s[43,44,50] agree well with the simple models, especially (22), which was noted phenomenologically at the time without any formal or first-principles derivation.[41] Later experiments summarized in Fig. 4(d) include data[42] collected after the derivation of the 1D model.[9,10] In addition to reporting cleaner data, the data in Fig. 4(d) also exhibit two distinct modes following (22) or (24), but, notably, never (20). The "barriers" are end-hats at one or both axial ends of the cylindrical diode, which prevent current leakage and make the data closer to the theoretical limit. As expected, the data with barriers, which correspond to the condition with the minimum current leakage or maximum current stored in the gap, match most closely with (22).

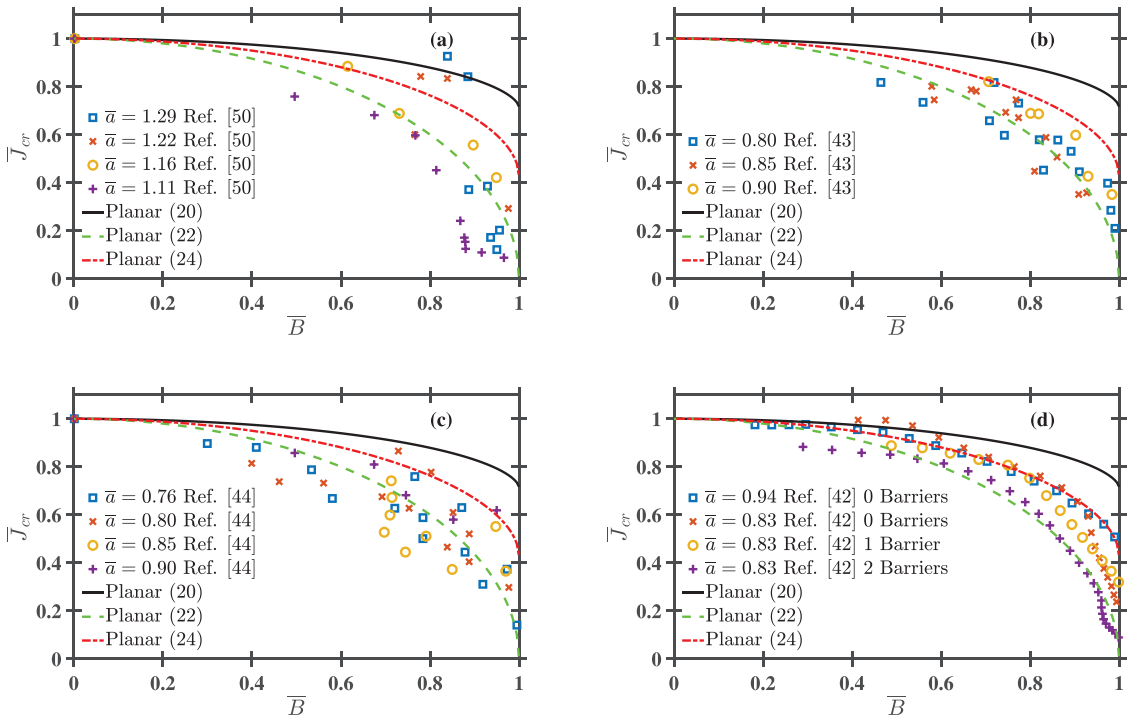

FIG. 4. Dimensionless current density $\overline{J}_{cr}$ as a function of dimensionless magnetic field $\overline{B}$. The data points in (a)–(d) are experimental data from Refs. 43, 44, 50, and, 42, respectively, where $\overline{a} = R_c/R_a$ is the ratio of the cathode-to-anode radii. The electron barriers in (d) are end-hats to prevent leakage current, similar to those depicted in Fig. 1. Since $\overline{a} \approx 1$ (near-planar), the experiments are compared to theoretical results from (20), (22), and (24).

First in chronological order, the data in Fig. 4(a) were produced by an inverse configuration magnetron, 2.42 cm radius cathode with the specified gap distances and voltages around 160 kV.[50] With mostly identical parameters, Ref. 43 changed to a standard configuration with 2.22 cm constant anode radius to obtain the smoother data shown in Fig. 4(b). The authors conjectured that the data and theory for these two data sets differed due to electron self-fields; since the electron flow was weakly relativistic,[43] these self-fields may cause the excellent match between the simple model and experimental results. Since the self-field explanation was insufficient to explain the deviations from the 1D model extant in the literature at the time, the final paper in this series, shown in Fig. 4(c), offered a self-described "back of the envelope" equation $J_{cr} \propto \left[1-(B/B_H)^2\right]^{1/2}$. Although they did not provide any physical explanation for this scaling,[44] it is identical to the relationship we have derived simply (22). The final experiment, which used a conventional cylindrical magnetron with a 5 cm radius cathode, 3 and 10 mm gaps, and much lower voltages (no more than tens of kV),[42] is reported in Fig. 4(d), and as conducted much later with the benefit of the most recent, prior 1D model[9,10] for validation. The experiment included electron barriers, more commonly called end-hats, in some 10 mm experiments to lower current leakage.[44] End-hats are commonly used in crossed-field electron devices to provide electrostatic confinement in the direction of the magnetic field.[58] Again, (22) is largely upheld although (24) seems to be a possible, true upper limit for these experiments in all cases.

The bounds on mismatch between theory and experiment are summarized in Table I, calculated as the difference between theoretical $\overline{J}_{cr}$ and experimental or simulation results, given by $\overline{J}_M = \overline{J}_{cr} - \overline{J}_{cr,x}$, where $\overline{J}_M$ is the mismatch normalized to Child–Langmuir, and $\overline{J}_{cr,x}$ represents either experimental ($x = \exp$) or simulation ($x = sim$) results. Since only one experimental curve each follows (22) and (24) in Fig. 4(d), they are not considered separately as any individual data set may be an outlier. Inspection of Fig. 4 implies that the maximum mismatch magnitude is greatest for (20) and least for (22), though (24) is less likely than (22) to underestimate experimental data, as may be expected since (24) was derived to be a maximum limit on crossed-field SCLC. Also, (22) is the only model to consistently bracket the experimental data; often, (20) and (24) largely overestimate $\overline{J}_{cr}$. The ranges between upper and lower mismatches generally match between (20), (22), and (24) since those depend primarily upon the variance in the experimental data itself. However, the range is not totally independent of fit; (20) always has the largest range, while (22) has the smallest except for Ref. 44, which has the narrowest range with (24). This most likely occurs since the greatest mismatch always occurs as $\overline{B} \to 1$, where (22) and (24) have distinct advantages. Expressed another way, (22) reduces the maximum magnitude of $\overline{J}_M$—that is, $|\overline{J}_M|_{\max}$—with regard to experimental data by 43%–68% compared to (20), while (24) reduces $|\overline{J}_M|_{\max}$ by 21%–42% compared to (20).

The 1D theory was validated by the 1D spatial and 3D velocity (1d3v) particle-in-cell (PIC) code XPDP1.[10,33,36–38,53] The agreement between simulation and theory and the disagreement with experimental results indicate that the theory and simulations do not adequately represent the physical reality of the four crossed-field experimental diodes considered.[42–44,50] The variational calculus extension to cylindrical geometry (21) has not improved predictions enough; to investigate this further, we conducted fully three dimensional (3D) simulations of both planar and cylindrical diodes described in Sec. II B.

Figure 5 shows that our simulations agree much better with experiment for $\overline{B} < 1$, while validating planar theory (20)[10] for $\overline{B} > 1$. By using the $\overline{J}_{cr}$ normalization (identical geometry at $\overline{B} = 0.6$), the effect of the magnetic field is nearly identical between planar in Fig. 5(a) and $\overline{a} = 2$ in Fig. 5(b), as demonstrated by Fig. 2. By nature, the $\hat{\theta}$ direction in cylindrical simulations is infinite; this, combined with using end-hats to reduce the impact of the finite z dimension in the simulation, results in a closer match between theory and simulation for the near-planar cylindrical geometry. In essence, a near-planar cylindrical geometry with end-hats allows the stored current to build up sufficiently to drive $\overline{J}_{cr}$ to zero as $\overline{B} \to \overline{B}_H^-$.

This motivates a much more careful study and design of experimental crossed-field diodes, especially those operating at $\overline{B} < 1$. Table I shows the bounds on $\overline{J}_M$ between theory and planar simulations for $\overline{B} < 1$, demonstrating the improvement of the simple theories (22) and (24) over (20), which always overestimates the simulation data.

We hypothesize that the failure of (20,21) and existing 1D planar theory[9,10] to represent $\overline{B} < 1$ while seeming to correctly predict $\overline{B} > 1$ data lies in the failure of one-dimensionalized models to adequately account for turbulence and gyration in the cathode-to-anode electron paths. The fully 3D simulations, unlike 1d3v simulations that agree well with 1D planar theory, can accurately account for this additional behavior, particularly motion in the directions orthogonal to the anode-cathode gap. These alter the force on the electron in the direction across the gap; any increase in the electric field due to binormal, stored current will increase transit time, resulting in a decreased space-charge limit. In fact, as $\overline{B} \to 1$, the electron only asymptotically approaches the anode, which implies infinite transit time and infinite stored current (in the steady state).

The effect of cylindrical geometry is important for designing both conventional and inverted magnetrons. By varying $\overline{a}$ for several fixed values of $\overline{B}$ (including $\overline{B} = 0$), Fig. 6 considers conventional geometry ($\overline{a} < 1$ or $\overline{R}_c < \overline{R}_a$), inverted geometry ($\overline{a} > 1$ or $\overline{R}_c > \overline{R}_a$), and the planar limit ($\overline{a} \to 1$). For comparison, Fig. 6(a) also considers the Langmuir-Blodgett equation, the first cylindrical solution to SCLE.[5] To more clearly demonstrate the geometric effects, Fig. 6(b) shows

TABLE I. Mismatch $\overline{J}_M$ between planar theories and experimental/simulation critical Current density. ($\overline{J}_M = \overline{J}_{cr,theory} - \overline{J}_{exp\,or\,sim}$).

Data source	$\overline{J}_M$ with (20)	$\overline{J}_M$ with (22)	$\overline{J}_M$ with (24)
Reference 50, Fig. 4(a)	[−0.06, +0.72]	[−0.38, +0.35]	[−0.20, +0.57]
Reference 43, Fig. 4(b)	[+0.09, +0.53]	[−0.17, +0.14]	[+0.00, +0.31]
Reference 44, Fig. 4(c)	[+0.04, +0.59]	[−0.31, +0.22]	[−0.05, +0.36]
Reference 42, Fig. 4(d)	[−0.03, +0.64]	[−0.36, +0.10]	[−0.07, +0.41]
Planar simulations Fig. 5(a)	[+0.01, +0.67]	[−0.32, +0.11]	[−0.10, +0.42]

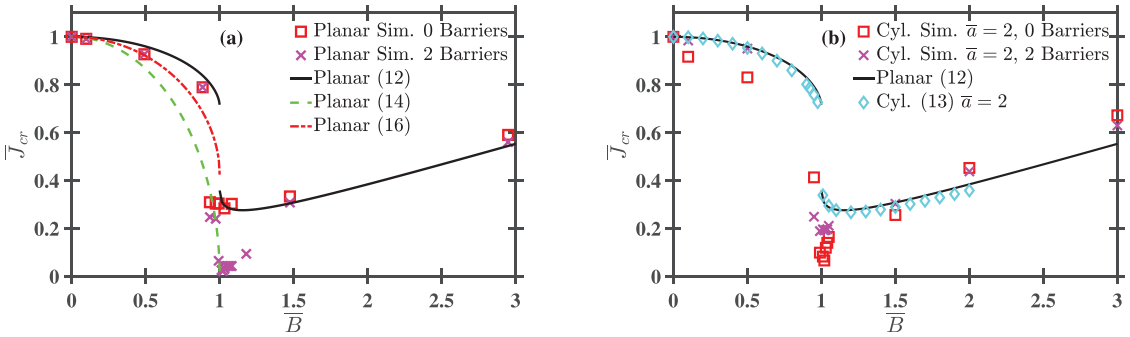

FIG. 5. Dimensionless current density $\overline{J}_{cr}$ as a function of dimensionless magnetic field $\overline{B}$. The data points in (a) and (b) are CST Particle Studio simulation results for planar and cylindrical geometries, respectively, where $\overline{a} = R_c/R_a$ is the ratio of the cathode-to-anode radii. The barriers are the end-hats shown in Fig. 1. (a) Comparison of planar simulations with no or two barriers to planar theory from (20), (22), and (24). (b) Comparison of cylindrical simulations with $\overline{a} = 2$ and either no or two end-hats to planar theory from (20) or cylindrical theory from (21). The cylindrical theory calculations are numerically unstable for approximately $0.95 \lesssim \overline{B} \lesssim 1.05$.

normalized results for the same data from Fig. 6(a). Extreme $\overline{a}$ always reduces $\overline{J}_{cr}$, especially for $\overline{B} \approx 1$—note that the divot for $\overline{B} > 1$ in Fig. 1 occurs for all $\overline{a}$ calculated.

IV. CONCLUSION

We have derived a theory for SCLC for a crossed-field diode for magnetic fields both $B < B_H$ and $B > B_H$ for planar and cylindrical diodes using the principles of variational calculus. The variational model from (18)–(20) is fully analytic except that solving for the cylindrical geometry for $B > B_H$ requires numerically solving for the maximum electron excursion distance (Brillouin hub height). Although not amenable to a closed form solution, the variational model gives the same results as previous one dimensional (1D) models[9,10] and extensions to cylindrical diodes; however, experimental data show a clear deviation as $B \to B_H^-$.[42–44,50] This motivated the derivation of several simple analytic models to capture this experimental behavior. We hypothesize that the simple and full models differ due to multi-dimensionality, small magnetic field misalignments due to experiment construction or self-magnetic fields from weakly relativistic flows. Fully three-dimensional simulations confirm the experimental results over prior models for the first time due in large part to replicating important two-dimensional design elements such as end-hats.

Future work will incorporate multi-dimensionality into the electron force law and consider arbitrary magnetic fields that include a component parallel to the electric field.[29,38] Conformal mapping, which has been applied to solve for SCLC for nonstandard geometries with no magnetic fields,[56] may also be useful for solving for crossed-field SCLC for more realistic geometries by transforming them into convenient planes or cylinders. Conformal mapping also provides the advantage of being strictly geometric in nature, which could allow direct translation of multi-dimensional effects to other geometries once they are obtained for a planar diode. Moreover, real crossed-field devices are non-ideal, so incorporating external circuit resistors to represent losses,[37] axial magnetic tilt,[38] or alternating current bias instabilities[36] into the variational (or conformal) model may provide further insight into the SCLC behavior of non-planar geometries and further facilitate the reconciliation of prior planar solutions and variational models to appropriately account for these physical complications. The effect of dissipative forces due to collisions or plasma oscillations may have similar, perturbative effects upon crossed-field SCLC and will be investigated; we conjecture that collisions will cause electrons to

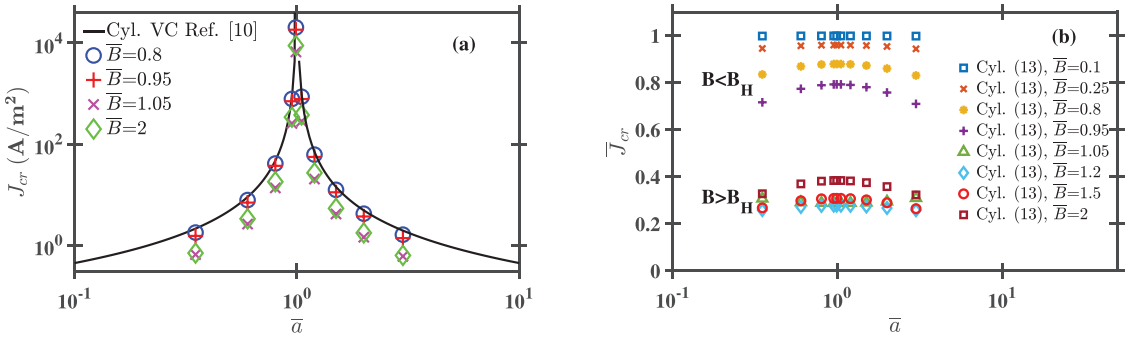

FIG. 6. (a) Space-charge limited current density J_{cr} as a function of the ratio of cathode-to-anode radius $\overline{a} = R_c/R_a$ for non-magnetic diodes using variational calculus (VC)[6] and the Langmuir–Blodgett (LB)—equation[5] for non-magnetic cylindrical diodes and (21) for several values of dimensionless magnetic field for cylindrical crossed-field diodes. (b) Dimensionless space-charge limited current density for a cylindrical crossed-field diode as a function of using (21) for various. We include borderline calculations; for $\overline{a} \gg 1$ or $\overline{a} \ll 1$, (21) becomes numerically unstable for $0.95 \lesssim \overline{B} \lesssim 1.05$.

remain in the gap longer, contributing more space-charge with lower critical current. Ultimately, experiments with simple diode designs may provide further insight into the utility of variational calculus (and, ultimately, conformal mapping) for potential application to more complicated and realistic geometries.

ACKNOWLEDGMENTS

This material is based upon the work supported by the Air Force Office of Scientific Research under Award No. FA9550-19-1-0101.

APPENDIX A: LOCAL ONE-DIMENSIONAL CONTINUITY

When discussing continuity, one must carefully assess dimensionality[59]; typically, charge q is accounted for in three-dimensional (3D) space by

$$dq/dt + \oiint_S \vec{J} \cdot d\vec{S} = 0, \tag{A1}$$

with differential area vector $\vec{S}$ for the closed surface S. Equation (A1), which in 3D becomes the textbook continuity equation $\nabla \cdot \vec{J} = 0$, is not universal for one- and two-dimensional (1D and 2D) systems since the differential volume is non-constant for non-Cartesian geometries.

For general coordinates $\vec{x} = (x_1, x_2, x_3)$, the general differential form of (A1) in the x_1 direction is

$$\nabla \cdot \left(\overline{\chi}(\vec{x})\rho\vec{v}\right) = \nabla \cdot \left(\overline{\chi}(\vec{x})\vec{J}\right) = 0, \tag{A2}$$

where $\overline{\chi}(\vec{x}) = \Delta x_2(\vec{x})\Delta x_3(\vec{x})$, for 1D systems, with x_2 and x_3 are orthogonal to the x_1 flow, $\overline{\chi} = 1$, r, and r^2, for 1D planar, cylindrical, and spherical geometries, respectively.[55] Applying (A2) to the $B = 0$ forms of SCLC[6] shows continuity is satisfied.[59] For example, for concentric cylinders and $B = 0$, we obtain.

$$J_c(r) = \frac{4V_g^{3/2}\epsilon_0\sqrt{2e/m}}{9r^2(\ln\overline{a})^2}, \tag{A3}$$

which we evaluate at $r = R_C$ to determine SCLC.[6] Substituting (A3) into (A2) with cylindrical $\overline{\chi}(\vec{x}) = r$ yields

$$\nabla \cdot \left(\overline{\chi}(\vec{x})\vec{J}\right) = \nabla \cdot \left(r\left[\frac{4V_g^{\frac{3}{2}}\epsilon_0\sqrt{\frac{2e}{m}}}{9r^2(\ln\overline{a})^2}\right]\hat{r}\right) = \frac{1}{r}\frac{\partial\left[r\left(r\frac{4V_g^{\frac{3}{2}}\epsilon_0\sqrt{\frac{2e}{m}}}{9r^2(\ln\overline{a})^2}\right)\right]}{\partial r} = 0, \tag{A4}$$

which verifies (A2) for the cylindrical geometry.

APPENDIX B: EULER–LAGRANGE EQUATION DERIVATIONS

This appendix outlines the steps necessary to derive (18) and (19). We first reiterate the planar integrand (15) as

$$f = \phi_{xx}\left[\frac{2e\phi}{m} - \Omega^2x^2\right]^{1/2}. \tag{B1}$$

Carrying out the derivatives for the first term of (17) yields

$$\left(\frac{\partial f}{\partial \phi_{xx}}\right) = \left[\frac{2e\phi}{m} - \Omega^2x^2\right]^{1/2}, \tag{B2}$$

$$\frac{\partial}{\partial x}\left(\frac{\partial f}{\partial \phi_{xx}}\right) = \left[\frac{2e\phi}{m} - \Omega^2x^2\right]^{-1/2}\left(\frac{e\phi_x}{m} - \Omega^2x\right), \tag{B3}$$

$$\frac{\partial^2}{\partial x^2}\left(\frac{\partial f}{\partial \phi_{xx}}\right) = \left[\frac{2e\phi}{m} - \Omega^2x^2\right]^{-1/2}\left(\frac{e\phi_{xx}}{m} - \Omega^2\right) - \left[\frac{2e\phi}{m} - \Omega^2x^2\right]^{-3/2}\left(\frac{e\phi_x}{m} - \Omega^2x\right)^2. \tag{B4}$$

Carrying out the relevant operations for the second term of (17) gives

$$\frac{\partial}{\partial x}\left(\frac{\partial f}{\partial \phi_x}\right) = 0. \tag{B5}$$

The derivative for the third term of (17) is

$$\left(\frac{\partial f}{\partial \phi}\right) = \frac{e}{m}\phi_{xx}\left[\frac{2e\phi}{m} - \Omega^2x^2\right]^{-1/2}. \tag{B6}$$

Combining (B4)–(B6) and multiplying through by $(m/e)\left[2e\phi/m - \Omega^2x^2\right]^{1/2}$ yields

$$\left(2\phi_{xx} - \frac{m}{e}\Omega^2\right) = \frac{m}{e}\left[\frac{2e\phi}{m} - \Omega^2x^2\right]^{-1}\left(\frac{e\phi_x}{m} - \Omega^2x\right)^2. \tag{B7}$$

Isolating ϕ_{xx} in (B7) gives (note $\phi_{xx} \equiv \nabla^2\phi$ in 1D planar)

$$\phi_{xx} = \frac{\phi_x^2 - 2B\Omega\phi_x x + 4\phi B\Omega}{4\phi - 2B\Omega x^2}, \tag{B8}$$

which is (18).

For the cylindrical integrand, we start from (16), given by

$$f = (r\phi_{rr} + \phi_r)\left[\frac{2e\phi}{m} - \frac{\Omega^2r^2}{4}\left(1 - 2\frac{R_c^2}{r^2} + \frac{R_c^4}{r^4}\right)\right]^{1/2}. \tag{B9}$$

In cylindrical coordinates, the first term of (17) is given by

$$\left(\frac{\partial f}{\partial \phi_{rr}}\right) = r\left[\frac{2e\phi}{m} - \frac{\Omega^2r^2}{4}\left(1 - 2\frac{R_c^2}{r^2} + \frac{R_c^4}{r^4}\right)\right]^{1/2}, \tag{B10}$$

$$\frac{\partial}{\partial r}\left(\frac{\partial f}{\partial \phi_{rr}}\right) = r\left[\frac{2e\phi}{m} - \frac{\Omega^2r^2}{4}\left(1 - 2\frac{R_c^2}{r^2} + \frac{R_c^4}{r^4}\right)\right]^{-1/2} \times \left(\frac{e}{m}\phi_r - \frac{\Omega^2r}{4} + \frac{\Omega^2R_c^4}{4r^3}\right) + \left[\frac{2e\phi}{m} - \frac{\Omega^2r^2}{4}\left(1 - 2\frac{R_c^2}{r^2} + \frac{R_c^4}{r^4}\right)\right]^{1/2}. \tag{B11}$$

The last term on the right-hand side (RHS) of (B11) cancels with the second term from (17), given by

$$\frac{\partial}{\partial r}\left(\frac{\partial f}{\partial \phi_r}\right) = \left[\frac{2e\phi}{m} - \frac{\Omega^2 r^2}{4}\left(1 - 2\frac{R_c^2}{r^2} + \frac{R_c^4}{r^4}\right)\right]^{1/2}. \tag{B12}$$

Continuing the differentiation of (B11) with the final term on the RHS removed yields

$$\begin{aligned}\frac{\partial^2}{\partial r^2}\left(\frac{\partial f}{\partial \phi_{rr}}\right) = &-r\left[\frac{2e\phi}{m} - \frac{\Omega^2 r^2}{4}\left(1 - 2\frac{R_c^2}{r^2} + \frac{R_c^4}{r^4}\right)\right]^{-3/2} \\ &\times \left(\frac{e}{m}\phi_r - \frac{\Omega^2 r}{4} + \frac{\Omega^2 R_c^4}{4r^3}\right)^2 \\ &+ \left[\frac{2e\phi}{m} - \frac{\Omega^2 r^2}{4}\left(1 - 2\frac{R_c^2}{r^2} + \frac{R_c^4}{r^4}\right)\right]^{-1/2} \\ &\times \left(\frac{e}{m}\phi_r - \frac{\Omega^2 r}{4} + \frac{\Omega^2 R_c^4}{4r^3}\right) \\ &+ r\left[\frac{2e\phi}{m} - \frac{\Omega^2 r^2}{4}\left(1 - 2\frac{R_c^2}{r^2} + \frac{R_c^4}{r^4}\right)\right]^{-1/2} \\ &\times \left(\frac{e}{m}\phi_{rr} - \frac{\Omega^2}{4} - 3\frac{\Omega^2 R_c^4}{4r^4}\right).\end{aligned} \tag{B13}$$

The third term from (17) is

$$\left(\frac{\partial f}{\partial \phi}\right) = \frac{e}{m}(r\phi_{rr} + \phi_r)\left[\frac{2e\phi}{m} - \frac{\Omega^2 r^2}{4}\left(1 - 2\frac{R_c^2}{r^2} + \frac{R_c^4}{r^4}\right)\right]^{-1/2}. \tag{B14}$$

Combining (B13) and (B14) and multiplying through by $(m/e)\left[2e\phi/m - \Omega^2 r^2/4\left(1 - 2R_c^2/r^2 + R_c^4/r^4\right)\right]^{1/2}$ yields

$$\begin{aligned}(r\phi_{rr} + \phi_r) + \left(\phi_r - \frac{B\Omega r}{4} + \frac{B\Omega R_c^4}{4r^3}\right) + r\left(\phi_{rr} - \frac{B\Omega}{4} - 3\frac{B\Omega R_c^4}{4r^4}\right) \\ = r\left[2\phi - \frac{B\Omega r^2}{4}\left(1 - 2\frac{R_c^2}{r^2} + \frac{R_c^4}{r^4}\right)\right]^{-1}\left(\phi_r - \frac{B\Omega r}{4} + \frac{B\Omega R_c^4}{4r^3}\right)^2.\end{aligned} \tag{B15}$$

Identifying $\nabla^2\phi = \phi_{rr} + \phi_r/r$ for 1D cylindrical geometry allows us to simplify (B15) to obtain

$$\begin{aligned}2\nabla^2\phi - \frac{B\Omega}{2}\left(1 + \frac{R_c^4}{r^4}\right) = &\left[2\phi - \frac{B\Omega r^2}{4}\left(1 - 2\frac{R_c^2}{r^2} + \frac{R_c^4}{r^4}\right)\right]^{-1} \\ &\times \left(\phi_r - \frac{B\Omega r}{4}\left(1 - \frac{R_c^4}{r^4}\right)\right)^2.\end{aligned} \tag{B16}$$

Isolating $\nabla^2\phi$ in (B16) yields

$$\nabla^2\phi = \frac{\left(\phi_r - \frac{B\Omega r}{4}\left(1 - \frac{R_c^4}{r^4}\right)\right)^2 + \frac{B\Omega}{2}\left(1 + \frac{R_c^4}{r^4}\right)\left[2\phi - \frac{B\Omega r^2}{4}\left(1 - 2\frac{R_c^2}{r^2} + \frac{R_c^4}{r^4}\right)\right]}{4\phi - \frac{B\Omega r^2}{2}\left(1 - \frac{R_c^2}{r^2}\right)^2}. \tag{B17}$$

The complicated numerator on the RHS of (B17) may be expanded to obtain

$$\begin{aligned}\phi_r^2 - \frac{B\Omega r}{2}\phi_r\left(1 - \frac{R_c^4}{r^4}\right) + \left(\frac{B\Omega r}{4}\right)^2\left(1 - \frac{R_c^4}{r^4}\right)^2 \\ + \frac{B\Omega}{2}\left(1 + \frac{R_c^4}{r^4}\right)\left[2\phi - \frac{B\Omega r^2}{4}\left(1 - 2\frac{R_c^2}{r^2} + \frac{R_c^4}{r^4}\right)\right].\end{aligned} \tag{B18}$$

Rearranging (B18) gives

$$\begin{aligned}\phi_r^2 - r\phi_r\frac{B\Omega}{2}\left(1 - \frac{R_c^4}{r^4}\right) + B\Omega\phi\left(1 + \frac{R_c^4}{r^4}\right) + \left(\frac{B\Omega r}{4}\right)^2 \\ \times\left[1 - 2\frac{R_c^4}{r^4} + \frac{R_c^8}{r^8} - 2 - 2\frac{R_c^4}{r^4} + 4\frac{R_c^2}{r^2} + 4\frac{R_c^6}{r^6} - 2\frac{R_c^4}{r^4} - 2\frac{R_c^8}{r^8}\right].\end{aligned} \tag{B19}$$

From the binomial expansion, the term in (square brackets) in (B19) is $-\left[1 - (R_c/r)^2\right]^4$. Using (B19) in (B17) yields

$$\nabla^2\phi = \frac{\phi_r^2 - r\phi_r\frac{B\Omega}{2}\left(1 - \frac{R_c^4}{r^4}\right) + B\Omega\phi\left(1 + \frac{R_c^4}{r^4}\right) - \left(\frac{B\Omega r}{4}\right)^2\left[1 - \left(\frac{R_c}{r}\right)^2\right]^4}{4\phi - \frac{B\Omega}{2}r^2\left(1 - \frac{R_c^2}{r^2}\right)^2}, \tag{B20}$$

which is (19).

DATA AVAILABILITY

The data that support the findings of this study are available from the corresponding author upon reasonable request.

REFERENCES

[1]P. Zhang, A. Valfells, L. K. Ang, J. W. Luginsland, and Y. Y. Lau, "100 years of the physics of diodes," Appl. Phys. Rev. **4**, 011304 (2017).

[2]P. Zhang, Y. S. Ang, A. L. Garner, Á. Valfells, J. W. Luginsland, and L. K. Ang, "Space-charge limited current in nanodiodes: Ballistic, collisional and dynamical effects," J. Appl. Phys. **129**, 100902 (2021).
[3]A. L. Garner, G. Meng, Y. Fu, A. M. Loveless, R. S. Brayfield II, and A. M. Darr, "Transitions between electron emission and gas breakdown mechanisms across length and pressure scales," J. Appl. Phys. **128**, 210903 (2020).
[4]C. D. Child, "Discharge from hot CaO," Phys. Rev. **32**, 492–511 (1911).
[5]I. Langmuir, "The effect of space charge and residual gases on thermionic currents in high vacuum," Phys. Rev. **2**, 450–486 (1913).
[6]A. M. Darr and A. L. Garner, "A coordinate system invariant formulation for space-charge limited current in vacuum," Appl. Phys. Lett. **115**, 054101 (2019).
[7]A. W. Hull, "The effect of a uniform magnetic field on the motion of electrons between coaxial cylinders," Phys. Rev. **18**, 31–57 (1921).
[8]D. H. Simon, Y. Y. Lau, G. Greening, P. Wong, B. W. Hoff, and R. M. Gilgenbach, "Stability of Brillouin flow in planar, conventional, and inverted magnetrons," Phys. Plasmas **22**, 082104 (2015).
[9]Y. Y. Lau, P. J. Christenson, and D. Chernin, "Limiting current in a crossed-field gap," Phys. Fluids B **5**, 4486–4489 (1993).
[10]P. J. Christenson and Y. Y. Lau, "Transition to turbulence in a crossed-field gap," Phys. Plasmas **1**, 3725–3727 (1994).
[11]S. C. Exelby, G. B. Greening, N. M. Jordan, D. A. Packard, D. Simon, Y. Y. Lau, B. W. Hoff, and R. M. Gilgenbach, "High-power recirculating planar crossed-field amplifier design and development," IEEE Trans. Electron Devices **65**, 2361–2365 (2018).
[12]N. A. Masnari and J. E. Rowe, "Experimental characteristics of crossed-field space-charge flows," J. Appl. Phys. **37**, 1825–1830 (1966).
[13]R. P. Little, H. M. Ruppel, and S. T. Smith, "Beam noise in crossed electric and magnetic fields," J. Appl. Phys. **29**, 1376–1377 (1958).
[14]J. Browning, S. Fernandez-Gutierrez, M. C. Lin, D. N. Smithe, and J. Watrous, "Phase control and fast start-up of a magnetron using modulation of an addressable faceted cathode," Appl. Phys. Lett. **104**, 233507 (2014).
[15]L. Wu and L. K. Ang, "Low temperature refrigeration by electron emission in a crossed-field gap," Appl. Phys. Lett. **89**, 133503 (2006).
[16]M. S. Dincer, S. S. Tezcan, and H. Duzkaya, "Magnetic insulation in nitrogen subjected to crossed fields," AIP Adv. **8**, 095026 (2018).
[17]V. Nallasamy, S. K. Datta, S. U. Reddy, and P. K. Jain, "Advances and present trends in magnetically insulated line oscillator," J. Electromagn. Waves App. **31**, 1864–1874 (2017).
[18]M. Pearlman and J. Browning, "Simulation of a time-varying distributed cathode in a linear format crossed-field amplifier," IEEE Trans. Plasma Sci. **47**, 3960–3966 (2019).
[19]D. H. Simon, Y. Y. Lau, G. Greening, B. W. Hoff, P. Wong, and R. M. Gilgenbach, "Stability of Brillouin flow in slow-wave structure," Phys. Plasmas **23**, 092101 (2016).
[20]S. N. Abolmasov, "Physics and engineering of crossed-field discharge devices," Plasma Sources Sci. Technol. **21**, 035006 (2012).
[21]P. T. Kirstein and G. S. Kino, "Solution to the equations of space-charge flow by the method of separation of variables," J. Appl. Phys. **29**, 1758–1767 (1958).
[22]S. Marini, F. B. Rizzato, and R. Pakter, "Thermal effects and space-charge limited transitions in crossed-field devices," Phys. Plasmas **21**, 083111 (2014).
[23]D. M. MacGregor, "Computer simulation of the backward-wave distributed-emission crossed-field amplifier," IEEE Electron Device Lett. **7**, 134–136 (1980).
[24]C. W. Mendel, D. B. Seidel, and S. A. Slutz, "A general theory of magnetically insulated electron flow," Phys. Fluids **26**, 3628–3635 (1983).
[25]P. Zhao, L. Guo, and P. Shu, "Computational studies of suppression of microwave gas breakdown by crossed dc magnetic field using electron fluid model," Jpn. J. Appl. Phys., Part 1 **55**, 086001 (2016).
[26]K. L. Cartwright, P. J. Christenson, J. P. Verboncoeur, and C. K. Birdsall, "Surface wave enhanced collisionless transport in a bounded crossed-field nonneutral plasma," Phys. Plasmas **7**, 1740–1745 (2000).
[27]Y. M. Saveliev, W. Sibbett, and D. M. Parkes, "Self-excitation and operational characteristics of the crossed-field secondary emission electron source," Rev. Sci. Instrum. **70**, 4502–4514 (1999).
[28]Y. Hadas, A. Sayapin, Y. E. Krasik, V. Bernshtam, and I. Schnitzer, "Plasma dynamics during relativistic S-band magnetron operation," J. Appl. Phys. **104**, 064125 (2008).
[29]B. S. Stutzman and J. W. Luginsland, "Loss of magnetic insulation in a crossed-field diode: Ion and collisional effects," IEEE Trans. Plasma Sci. **38**, 2010–2015 (2010).
[30]W. S. Koh and L. K. Ang, "Two-dimensional space-charge-limited flows in a crossed-field gap," Appl. Phys. Lett. **90**, 141503 (2007).
[31]T. A. DeMassa and J. E. Rowe, "Space-charge and secondary emission effects in a computer simulation of crossed-field distributed-emission amplifiers," IEEE Trans. Electron Devices **15**, 85–97 (1968).
[32]L. K. Ang, T. J. T. Kwan, and Y. Y. Lau, "Limiting current density in a crossed-field nanogap," Phys. Rev. E **64**, 017501 (2001).
[33]J. P. Verboncoeur and C. K. Birdsall, "Rapid current transition in a crossed-field gap," Phys. Plasmas **3**, 712–713 (1996).
[34]Y. Y. Lau, J. W. Luginsland, K. L. Cartwright, and M. D. Haworth, "Role of ions in a crossed-field diode," Phys. Rev. Lett. **98**, 015002 (2007).
[35]M. Lopez, Y. Y. Lau, J. W. Luginsland, D. W. Jordan, and R. M. Gilgenbach, "Limiting current in a relativistic diode under the condition of magnetic insulation," Phys. Plasmas **10**, 4489–4493 (2003).
[36]P. J. Christenson and Y. Y. Lau, "One-dimensional modulational instability in a crossed-field gap," Phys. Rev. Lett. **76**, 3324–3327 (1996).
[37]P. J. Christenson, D. P. Chernin, A. L. Garner, and Y. Y. Lau, "Resistive destabilization of cycloidal electron flow and universality of (near-) Brillouin flow in a crossed-field gap," Phys. Plasmas **3**, 4455–4462 (1996).
[38]A. L. Garner, Y. Y. Lau, and D. Chernin, "Collapse of cycloidal electron flows induced by misalignments in a magnetically insulated diode," Phys. Plasmas **5**, 2447–2453 (1998).
[39]Y. Y. Lau, J. W. Luginsland, K. L. Cartwright, D. H. Simon, W. Tang, B. W. Hoff, and R. M. Gilgenbach, "A re-examination of the Buneman-Hartree condition in a cylindrical smooth-bore relativistic magnetron," Phys. Plasmas **17**, 033102 (2010).
[40]I. M. Rittersdorf, P. F. Ottinger, R. J. Allen, and J. W. Schumer, "Current density scaling expressions for a bipolar space-charge-limited cylindrical diode," IEEE Trans. Plasma Sci. **43**, 3626–3633 (2015).
[41]D. H. Simon, Y. Y. Lau, J. W. Luginsland, and R. M. Gilgenbach, "An unnoticed property of the cylindrical relativistic Brillouin flow," Phys. Plasmas **19**, 043103 (2012).
[42]B. H. Vanderberg and J. E. Eninger, "Measurement and interpretation of current transmission in a crossed-field diode below cutoff," Phys. Plasmas **4**, 256–258 (1997).
[43]T. J. Orzechowski and G. Bekefi, "Current flow in a high-voltage diode subjected to a crossed magnetic field," Phys. Fluids **19**, 43–51 (1976).
[44]T. J. Orzechowski and G. Bekefi, "Microwave emission from pulsed, relativistic e-beam diodes I. The smooth-bore magnetron," Phys. Fluids **22**, 978–985 (1979).
[45]K. D. Bergeron and J. W. Poukey, "Relativistic space-charge flow in a magnetic field," Appl. Phys. Lett. **27**, 58–60 (1975).
[46]J. P. VanDevender, T. D. Pointon, D. B. Seidel, K. W. Struve, C. Jennings, B. V. Oliver, and L. X. Schneider, "Requirements for self-magnetically insulated transmission lines," Phys. Rev. Spec. Top. Accel. Beams **18**, 030401 (2015).
[47]V. P. Gopinath and B. H. Vanderberg, "Reduction of crossed-field diode transmitted current due to anode secondary emission," Phys. Plasmas **5**, 261–265 (1998).
[48]V. P. Gopinath, J. P. Verboncoeur, and C. K. Birdsall, "Similarity of stability characteristics of planar and coaxial crossed-field devices," Phys. Plasmas **3**, 2766–2769 (1996).
[49]G. H. Goedecke, B. T. Davis, C. Chen, and C. B. Baker, "On steady flows in smooth-walled magnetrons: Fundamental modes and no-cutoff flows in planar geometry," Phys. Plasmas **12**, 113104 (2005).
[50]J. Golden, T. J. Orzechoswki, and G. Bekefi, "Magnetic insulation of an intense relativistic electron beam," J. Appl. Phys. **45**, 3211–3212 (1974).
[51]B. H. Vanderberg and J. E. Eninger, "Parametric scaling study of a magnetically insulated thermionic vacuum switch," IEEE Trans. Plasma Sci. **24**, 165–172 (1996).
[52]F. F. Chen, *Introduction to Plasma Physics and Controlled Fusion* (Springer, New York, 2016).
[53]B. van Brunt, *The Calculus of Variations* (Springer, New York, 2004).
[54]P. J. Christenson, "Equilibrium, stability, and turbulence in cycloidal electron flows in crossed electric and magnetic fields," Ph.D. dissertation (University of Michigan, 1996).

[55]Z. Chen, G. Huan, and Y. Ma, *Computational Methods for Multiphase Flows in Porous Media* (Siam, Philadelphia, 2006), p. 12.
[56]N. R. Sree Harsha and A. L. Garner, "Applying conformal mapping to derive analytical solutions of space-charge-limited current density for various geometries," IEEE Trans. Electron Devices **68**, 264–270 (2021).
[57]CP Studio, *CST Studio Suite* (CP Studio, Darmstadt, Germany, 2019).
[58]R. Bhattacharya, A. M. Darr, A. L. Garner, and J. Browning, "Analysis of injected electron beam propagation in a planar crossed-field gap," Appl. Sci. **11**, 2540 (2021).
[59]A. M. Darr, N. R. Sree Harsha, and A. L. Garner, "Response to "Comment on 'A coordinate system invariant formulation for space-charge limited current in vacuum'" [*Appl. Phys. Lett.* **118**, 266101 (2021)]," Appl. Phys. Lett. **118**, 266102 (2021).